Waveguiding Effect in the Gigahertz Frequency Range in Pillar-based Phononic-Crystal Slabs

Reza Pourabolghasem, Razi Dehghannasiri, Ali Asghar Eftekhar, and Ali Adibi*

School of Electrical and Computer Engineering, Georgia Institute of Technology, Atlanta, Georgia 30332, USA

(Received 25 June 2017; revised manuscript received 24 October 2017; published 12 January 2018)

The waveguiding effect for a phononic-crystal (PnC)-based device operating in the gigahertz (GHz) frequency regime is experimentally demonstrated. To that end, a metallic pillar-based PnC membrane with a PnC band gap in the GHz frequency range is designed, and, based on that, an acoustic waveguide operating in the GHz regime is designed and fabricated. To characterize the fabricated PnC waveguide, a set of focusing interdigital transducers is designed and fabricated, enabling efficient excitation and detection of acoustic signals inside the PnC waveguide. The finite-element method is used to study the acoustic properties of the proposed structures and optimize their design. Experimental evidence supporting the existence of the waveguiding effect in the proposed structure in the GHz frequency regime is provided, showing reasonable agreement with the numerical calculations.

DOI: 10.1103/PhysRevApplied.9.014013

I. INTRODUCTION

Pillar-based phononic-crystal (PnC) membranes are 2D periodic structures composed of metallic or nonmetallic pillars placed on the surface of a single- or multilayer membrane (see, e.g., Fig. 1). The acoustic properties of these structures, including phononic band gaps (PnBGs), which enable three-dimensional acoustic confinement in membranes, their local-resonance properties, and their potential to exhibit Bragg PnBGs, have been the subject of extensive theoretical and experimental studies in the last two decades [1–5]. Such properties make pillar-based PnC structures a potential alternative platform for ultra-high-frequency (UHF) signal processing, given the promising results demonstrated with hole-based PnC membrane devices for megahertz signal-processing applications [6,7]. Frequency-manipulating devices are the building blocks of such a platform, and utilizing PnBGs designed at the desired frequency can facilitate the development of more sophisticated signal processing modules such as frequency multiplexers/demultiplexers [8], delay lines, and filters.

Designing PnCs with UHF PnBGs are only the first step in developing a complete PnC-based signal-processing platform in this frequency regime. The next logical step is to develop the frequency-selective building blocks such as PnC resonators [7,9,10], along with the devices that can guide the acoustic waves inside a phononic line defect (i.e., a PnC waveguide [11–14]). These building blocks can be combined by coupling the acoustic waves between PnC waveguides [15], PnC resonators [16], or a combination of the two [8] to form all-phononic signal-processing systems.

Scaling PnC devices to operate in the UHF regime requires shrinking geometrical dimensions. This frequency scaling through geometry scaling may seem rather trivial; however, experimental demonstration of PnC waveguides and resonators in such an UHF regime is still a challenge. Additionally, efficient coupling of the acoustic energy generated by an acoustic transducer to the PnC waveguides in the system poses a design challenge at high frequencies. Several theoretical studies have shown that using a specialized PnC-based structure known as the gradient index (GRIN) waveguide can improve the coupling efficiency of a plane-wave source to a PnC-based waveguide [17–19].

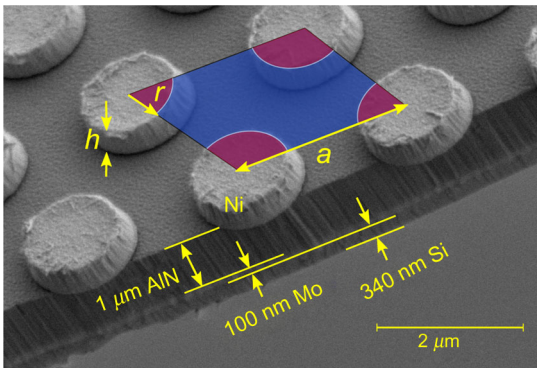

FIG. 1. Scanning-electron-microscope (SEM) image of a pillar-based PnC with a triangular lattice composed of Ni pillars on a three-layer membrane of AlN, Mo, and Si. The area outlined by the parallelogram illustrates a primitive unit cell of this lattice.

*Corresponding author.
ali.adibi@ece.gatech.edu

However, an effective GRIN waveguide relies on having a weakly anisotropic acoustic mode (i.e., an acoustic mode with almost-circular equal-frequency contours) [19]. This condition limits the feasibility of GRIN waveguides to certain polarizations within certain frequency ranges.

In this paper, we present a systematic method to address both challenges, i.e., (1) to design and demonstrate a PnC waveguide operating in the GHz frequency range, and (2) to design and demonstrate a piezoelectric transducer for efficient coupling of acoustic energy into a PnC waveguide at high frequencies. In Sec. II, we discuss our approach to design and fabricate a metallic pillar-based PnC membrane operating in the GHz frequency range. In Sec. III, we outline the design of the acoustic waveguide based on the developed GHz PnC. In Sec. IV, we explain the design of an alternative focusing interdigital transducer (IDT) to enable the efficient coupling of the acoustic energy into the aperture of a PnC waveguide [20–23]. Our fabrication details and experimental results are presented in Sec. IV. The final conclusions are drawn in Sec. V.

II. DESIGN OF A PILLAR-BASED PnC WITH GHz PHONONIC BAND GAP

The starting point for the design of a PnC-based waveguide is choosing an optimal PnC structure that supports a PnBG in the desired frequency range. Given our target frequency range (i.e., beyond 1 GHz), our focus is on optimizing a PnC structure that supports the widest PnBGs formed by the Bragg effect. Our previous study on the physics of the band-gap formation in pillar-based PnC membranes [4,5] suggests that using shorter pillars or pillars with reduced diameter leads to PnBGs at higher frequencies, but, at the same time, it results in a narrower PnBG and, eventually, closing of the band gap. Another geometrical parameter that can have a substantial effect on the center frequency of the PnBG is the lattice constant (a, specified in Fig. 1). As a single integrated phononic chip might house multiple PnC structures with different center frequencies, all of which have to share a common membrane, it is preferable to push the boundaries of what is possible by optimizing only the pillars—both their dimensions and their material properties—along with a conservative change to the lattice constant, without altering the membrane structure.

To design a PnC with the aforementioned properties and geometrical constraints, we use nickel (Ni) instead of gold (Au) as the metal of choice for the pillars. Ni is both lighter and stiffer (i.e., it has a lower density and a higher Young's modulus) and has lower acoustic-material loss compared to Au [24], pushing the center frequency of the PnBGs higher. Using Ni as the material of choice for the pillars, an exhaustive search is conducted over the height and radius of the pillars in the unit cell, and a lattice constant range of 1 ± 0.3 μm is allowed. This search results in the optimum PnC design shown in Fig. 1. As seen in this figure, the PnC of choice has a triangular lattice structure with Ni pillars on a three-layer membrane of aluminum nitride (AlN, 1 μm thick), molybdenum (Mo, 100 nm thick), and silicon (Si, 340 nm thick) from top to bottom [5]. The radius and the height of all pillars are 750 and 400 nm, respectively, and the lattice constant is $a = 2.5\,\mu$m.

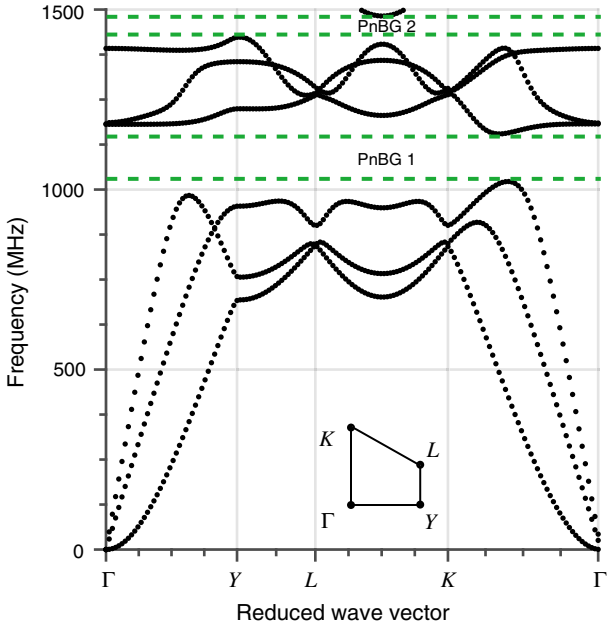

FIG. 2. Phononic band structure of the triangular pillar-based PnC membrane of Fig. 1 along the edges of the irreducible Brillouin zone of the PnC structure, as shown in the inset. The extents of the complete PnBGs are indicated by the dashed lines. The radius and the height of the Ni pillars are 750 and 400 nm, respectively. The thicknesses of AlN, Mo, and Si layers are 1 μm, 100 nm, and 340 nm, respectively. The lattice constant, a, is 2.5 μm.

The dispersion diagram of the designed PnC, calculated by the finite-element method (FEM) implemented in the COMSOL software package, is shown in Fig. 2, depicting the boundaries of a PnBG in the (1030–1155)-MHz frequency range (i.e., a gap-to-midgap ratio of 11.4%), along with a second narrower PnBG around 1450 MHz. The irreducible Brillouin zone of the structure (see the inset in Fig. 2) is derived by considering both the PnC lattice symmetry and the anisotropy of the Si layer in the membrane. As such, the Γ-Y, Γ-L, and Γ-K directions are not equivalent; hence, the irreducible Brillouin-zone boundary of Γ-Y-L-K is used. It should be noted that, based on our previous work on the physics of PnBG formation in pillar-based membrane PnCs [4], neither of these PnBGs is predominantly caused by the pillars' local-resonance effect. Because of the small height of the pillars relative to the PnC lattice constant ($h/a = 0.16$), the pillars' local resonance occurs at frequencies much higher than the PnBG frequencies caused predominantly by the Bragg scattering in the PnC, and changing the pillars' height does not drastically affect the position of the PnBG. For the purpose of this work, we will focus on utilizing the first PnBG due to its wider extent to form waveguides and resonators.

III. STRUCTURE AND DISPERSION DIAGRAM OF PnC-BASED WAVEGUIDES

To construct a waveguide from the PnC introduced in Sec. II, one may form a line defect by removing one column of pillars in the Γ-K direction from the perfect PnC lattice (see Fig. 3). This type of defect in the PnC lattice usually leads to guided or stationary modes confined inside the region without pillars, known as the *defect region*. The width of this region (the defect width, w, in Fig. 3) is a design parameter that can be changed to engineer the number and dispersion of the guided modes. To effectively simulate a PnC waveguide, we define a waveguide unit cell and apply Floquet boundary conditions (BCs) to two sides and the fixed BCs to the other two sides (as shown in Fig. 3) to model the periodicity and propagating nature of the elastic waves inside the defect region. It is important to note that, in this arrangement, the propagation direction of the guided modes will be along the y axis, as shown in Fig. 3. As such, we define the high-symmetry point Γ of this structure as corresponding to a Floquet BC phase of 0 rad, and the high-symmetry point X to a Floquet BC phase of π rad.

To calculate the dispersion diagram of this structure (for waves propagating in the y direction in Fig. 3), we sweep the Floquet BC phase from 0 rad to π rad with a step size of $\pi/40$ rad, and the eigenmodes of the structure are computed at each value of the Floquet phase using the FEM. To accurately tune the frequency of these confined modes, the waveguide defect width (w in Fig. 3) can be changed and the resulting dispersion diagram examined. The simulated dispersion diagrams for three PnC waveguides with different defect widths are shown in Figs. 4(a), 4(b), and 4(c). In each dispersion diagram, the modes inside the PnBG (i.e., 1030–1155 MHz) correspond to the guided acoustic modes of the PnC waveguide.

The importance of the defect width (i.e., w in Fig. 3) in engineering the number of guided modes and their dispersion is clear from Fig. 4. For a practical PnC waveguide, single-mode operation is highly desired. In addition, the polarization of the selected guided mode must be such that their excitation by an IDT is possible. Comparing the three PnC waveguides analyzed in Fig. 4, it is clear that the structure with $w = 0.8 \times a\sqrt{3}$ [see Fig. 4(b)] provides single-mode operation in the largest bandwidth (i.e., 1060–1080 MHz). One important fact to consider in designing PnC waveguides is that the polarization as well as the in-plane symmetry of the guided modes gradually changes as we sweep the wave number (k_y or, equivalently, the Floquet BC phase) from Γ to X. Specifically, the slanted oval in Fig. 4(b) shows a portion of the dispersion diagram of a guided mode with antisymmetric Lamb (AS)-type polarization that is also symmetric in plane. The displacement profile of the mode associated with a Floquet BC phase of 0.6756π rad in the Γ-X direction (corresponding to the frequency $f = 1067$ MHz) in Fig. 4(b) is shown in Fig. 5. The out-of-plane displacement of this mode and its lateral in-plane symmetry make the excitation and detection of the mode by IDTs straightforward. Another unique property of this eigenmode is that, in a reasonable range of frequencies (from 1060 to 1090 MHz), it is the only guided mode of the structure.

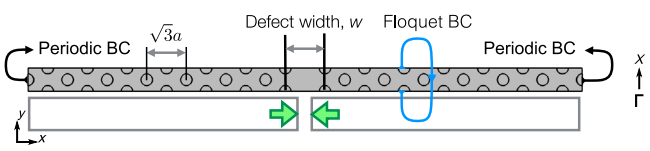

FIG. 3. Unit cell of a PnC waveguide based on a pillar-based PnC composed of pillars arranged in a triangular lattice. The boundary conditions (BCs) and the separation distance between the two PnC parts (or the defect width) are overlayed on the schematic of the structure for a PnC waveguide formed by removing one column of pillars from a perfect PnC ($w = \sqrt{3}a$, with a being the lattice constant). The propagation direction of the confined guided wave is along the Γ-X direction (in the k domain) or the y direction (in the real domain), both of which are illustrated in the figure.

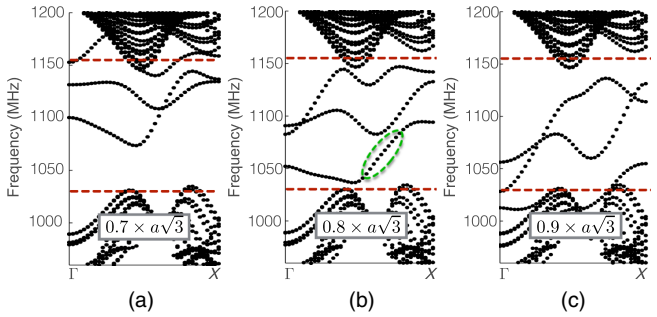

FIG. 4. Dispersion diagram of the PnC waveguide in Fig. 3 for defect widths of (a) $0.7 \times a\sqrt{3}$, (b) $0.8 \times a\sqrt{3}$, and (c) $0.9 \times a\sqrt{3}$. Dashed horizontal lines show the boundaries of the PnBG in the original PnC. The structure and the geometric dimensions of the underlying PnC are the same as those in Fig. 1.

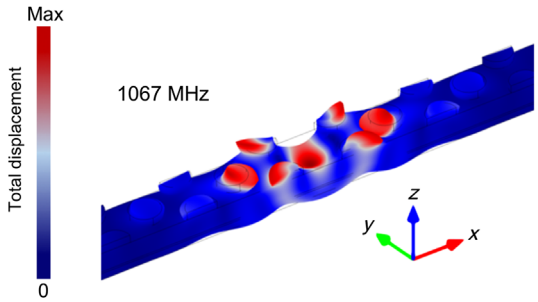

FIG. 5. Displacement profile of the guided mode, with AS polarization, of the membrane PnC waveguide, the dispersion diagram of which is shown in Fig. 4(b). The defect width is $w = 0.8 \times a\sqrt{3}$. The phase difference associated with the Floquet boundary condition is 0.6756π rad in the Γ-X direction.

It should be noted that the other modes (other than those inside the slanted oval region) are either of the shear-horizontal (SH) type or they are in-plane antisymmetric [5]. Unable to be excited by the surrounding IDTs, these waveguide modes fall in the deaf band of the device [25–27]. Based on theses properties, we choose the PnC waveguide with $w = 0.8 \times \sqrt{3}a$ [the structure corresponding to Fig. 4(b)] as the optimal structure to experimentally demonstrate the waveguiding effect.

IV. DESIGN OF FOCUSING IDTS FOR COUPLING ELASTIC WAVES TO PnC WAVEGUIDES

Figure 6(a) shows the structure for experimentally studying a PnC waveguide. A key requirement in this structure is the ability to focus the elastic energy onto a small opening corresponding to the guiding region of the PnC waveguide. A similar device needs to be designed for the case where the PnC waveguide replaced by a defect-free PnC [see Fig. 6(b)] to compare the transmission of the elastic wave to the designed polarization and the desired frequency to that of the PnC waveguide. This focusing requirement makes the design of IDTs more complex. In contrast to flat-aperture IDTs that are conventionally used to excite plane waves, focusing IDTs are usually formed by curved electrodes, as seen in Fig. 6(a). Similar focusing IDTs are also needed at the output of the structure to efficiently collect the elastic waves out of a PnC waveguide [see Fig. 6(a)].

Several methods can be envisioned for designing a focusing IDT, including, but not limited to, calculating the phase velocity of the desired elastic wave (with the desired polarization) at the desired operating frequency and calculating the corresponding phase front (i.e., equiphase contours) for a point source (emanating elastic waves from the focal point of the focusing IDT). By matching the location of the IDT electrodes (or fingers) to these equiphase contours, we can design a focusing IDT that meets the design criteria. However, this approach has certain limitations. First, the assumption of a pure polarization emanating from the focal point of the IDT is not correct for most PnC waveguide modes of interest, as these guided modes have (in most cases) a hybrid of different polarizations. Second, this design process uses an approximation of the ray-tracing models from a point source in the far field, but it neglects the near-field effects of the point source. Therefore, it limits our ability to design a focusing IDT close to its focal point to make the designed devices more compact.

To address the aforementioned limitations, we develop a systematic design method for focusing IDTs that relies on calculating the equiphase contours of the elastic wave generated by the mode of a truncated waveguide with its actual polarization—instead of a single-polarization point source—using the FEM simulations. In addition to enabling near-field calculations of the displacement profile, this approach account for the hybrid polarization of the waveguide mode as it enters the half-space (i.e., the membrane region outside the waveguide boundaries).

The phase-front calculation for the design of focusing IDTs involves two separate FEM simulations. The first step is an eigenmode analysis of the PnC waveguide structure with the desired phase for the Floquet boundary condition followed by an export of the displacement profile of the cross section of the waveguide. This displacement profile is used in the second simulation as the displacement boundary condition for the half-space, in which a half-circular domain with the perfectly matched layer (PML) at the outer radius is modeled.

In the rest of this section, we use the waveguide mode shown in Fig. 5 [for the PnC waveguide in Fig. 4(b)] as the basis of our focusing-IDT design. As such, we expect the designed IDTs to attain their maximum frequency response around the frequency of the target waveguide mode at 1067 MHz. Figure 7 shows how the displacement profile from the eigenmode analysis of the waveguide unit cell is mapped onto the boundary of the half-space. It should be noted that the displacement values extracted from the eigenmode analysis of the waveguide unit cell are treated as phasors; hence, the boundary condition for the displacement phasor is formulated accordingly.

After the boundary condition is applied, the second simulation, which is a frequency-domain analysis, is performed to calculate the steady-state response for the half-space when exposed to the exiting PnC waveguide mode profile at the desired frequency. Note that this simulation is a single-frequency simulation at the same

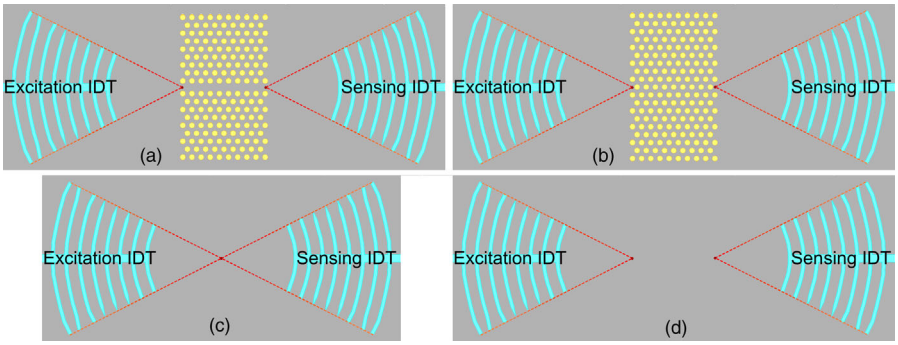

FIG. 6. Arrangement of the excitation and sensing focusing IDTs with (a) the PnC waveguide and (b) the PnC in between. Arrangement of (c) the near- and (d) far-focusing IDTs in the fabricated devices. The intersection of the dashed lines in all figures show the focal point of the corresponding focusing IDTs.

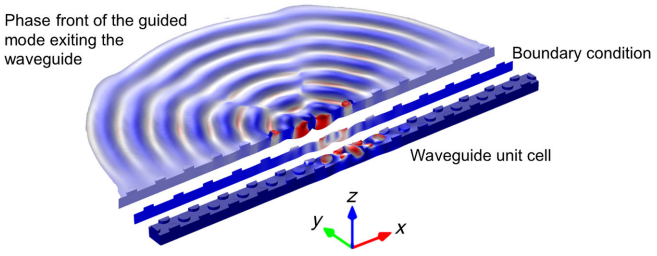

FIG. 7. Displacement profile of the guided mode at the exit of the PnC waveguide. The displacement profile of the eigenmode of the PnC waveguide unit cell is extracted and applied to the boundary of the half-space as its driving boundary condition. The outer shell of the half-space (seen as the half-circular domain) is surrounded by the PML (see Fig. 8).

frequency as that of the eigenmode from which the boundary condition is extracted. The peaks and valleys of the diffracted wave in the half-space as calculated by the frequency-response simulations are shown in Fig. 8.

Postsimulation processing of the displacement profile in Fig. 8 reveals the exact location of the peak contours and their distance. The peak contours are used to design the positions and the shapes of the IDT electrodes. As we use a Mo ground layer at the bottom of the AlN layer, the locations of the valley contours are not needed. The distance of these contours is used to design the width of the electrodes of the IDTs. As seen in Fig. 8, the phase front in the half-space has a distinct diffraction pattern resulting in slight aberrations in the peak contours of the displacement profile. To simplify the fabrication process and ensure the connectivity of the IDT electrodes, we decide to use only the middle part of the phase front for designing focusing IDTs, leading to the overlaid pattern of the IDT shown in Fig. 8.

To investigate the properties of the focusing IDTs, we also design and fabricate two pairs of focusing IDTs. The first pair is the same as those shown in Fig. 6(a) with the PnC waveguide removed from the middle, while the second pair is similar to the arrangement of the first pair, with their

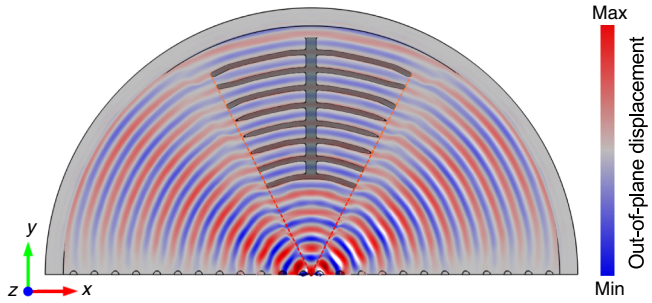

FIG. 8. Equiphase fronts of the guided mode of the PnC waveguide after exiting the waveguide. The driving boundary condition is applied to the bottom of the structure. The outer shell of the half circle is surrounded by the PML. The layout of the derived focusing IDT is overlaid on the displacement profile, and its azimuthal extent is indicated by the red dashed line.

distances changed such that the focal points of the excitation and sensing IDTs coincide [see Figs. 6(c) and 6(d)]. We refer to the former as the "far IDTs" and the later as the "near IDTs," as shown in Figs. 6(c) and 6(d), respectively. Comparing the measured transmission (S_{21}) of these two sets of IDTs helps us to understand the effectiveness of the focusing phenomenon augmented by the design of the IDTs. We expect to observe a much larger S_{21} for near IDTs than for far IDTs. Additionally, we expect that putting a waveguide between the far IDTs [as shown in Fig. 6(a)] will result in an improved S_{21} measurement as the waveguide starts at one focal point and ends at the other.

V. FABRICATION AND CHARACTERIZATION OF THE PnC-BASED WAVEGUIDES

A. Fabrication process

To fabricate the PnC waveguide device and the corresponding reference device [see Figs. 6(a) and 6(b)] along with the input, the output, and the PnC structure, we start with a Si-on-insulator wafer with layers of Mo (100 nm thick) and AlN (1 μm thick) deposited on top by Tegal Corporation (Fig. 1). Using photolithography with a silicon dioxide (SiO_2) hard mask, wide openings in the AlN are etched to enable the electrical contact, with the bottom Mo layer acting as the ground layer. The top electrodes are patterned by electron-beam lithography (EBL) using PMMA as the electron-beam resist, followed by the electron-beam evaporation of the chromium (Cr, 5 nm thick), as the adhesion layer, and aluminium (Al, 80 nm thick) and the lift-off process. Deposition of Ni pillars was conducted in a similar way to that of Al electrodes (i.e., using EBL, Cr/Ni deposition, and lift-off). It should be noted that the evaporation schedule of Ni is optimized to avoid damaging the underlying PMMA resist. Releasing the PnC membrane using the backside-alignment photolithography, Bosch process, and wet etching the buried oxide layer are performed similar to the steps outlined in our previous work [5]. Figures 9(a) and 9(b) show the SEM images of the fabricated waveguide structure and PnC with their corresponding input and output focusing IDTs, respectively. Close-up SEM images of the fabricated focusing IDT and the PnC waveguide are shown in Figs. 9(c) and 9(d), respectively.

B. Characterization results

We measure the S_{21} scattering parameter of the fabricated devices using an HP 8753D network analyzer. In all of our measurements, we use an averaging factor of at least 500 to reduce the noise, enabling the characterization of very low signal levels (down to −120 dB). With regard to electrical-port definitions of the IDTs, it is important to note that the electrodes on the structure, as shown in Fig. 6, are connected to the signal port of the network analyzer, while the underlying Mo layer is connected to the ground port.

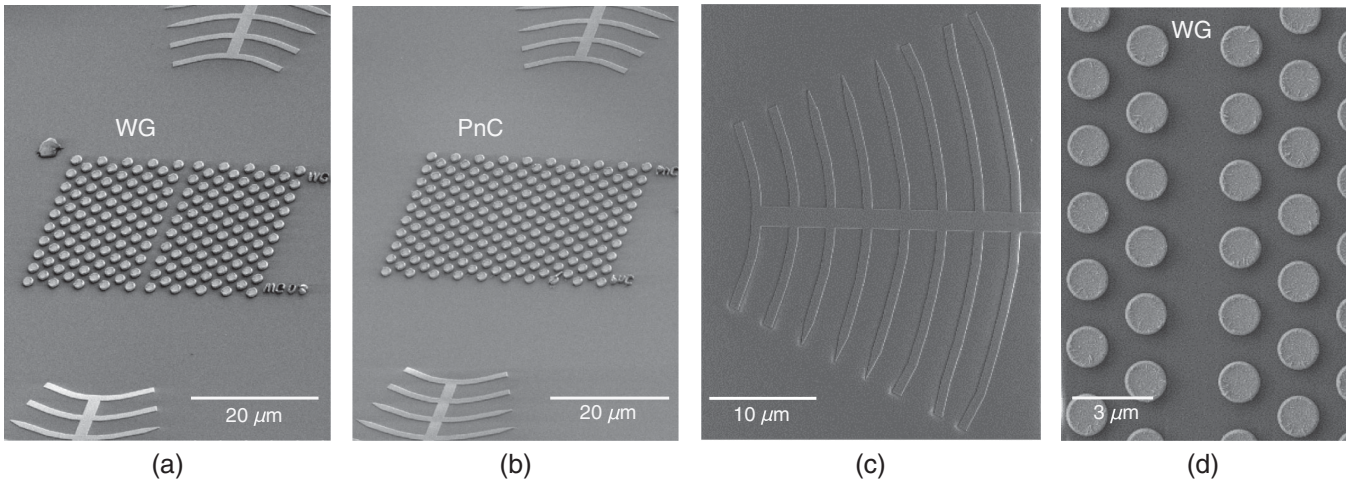

FIG. 9. SEM images of (a) the PnC waveguide structure and (b) a PnC with input and output focusing IDTs on the sides. (c) SEM image of the fabricated focusing IDT. (d) SEM image of the guiding region of the fabricated waveguide structure. The geometrical properties of the PnC structure are the same as those in Fig. 1.

To benchmark the waveguiding effect, we compare the measured S_{21} parameter of the device in Fig. 9(a) to that of a reference device in Fig. 9(b), both consisting of nine lattice periods along the direction of the wave propagation. The reference device is similar to the waveguide with the waveguide structure replaced with the same number of layers of the corresponding PnC structure. We expect the waveguide to show higher transmission around the frequency of the guided mode and demonstrate similar transmission values to that of the defect-free PnC at frequencies farther from the guiding region. As discussed earlier, the guided modes of interest are the eigenmodes surrounded by the slanted oval in Fig. 4(b).

Figure 10(a) shows the measured S_{21} parameter for the near and far IDTs (as defined in Sec. IV) in the (1000–1150)-MHz frequency range, with the operating frequency of the focusing IDTs tuned to a specific eigenmode of the waveguide at 1067 MHz. As expected, the near IDT attains its maximum transmission in the (1040–1060)-MHz frequency range, which is within 2.5% of the target frequency for a maximum transmission of 1067 MHz. We also observe, from Fig. 10(a), that when the focal points of the IDTs are not overlapping (i.e., far IDTs), the transmission drops by at least 7 dB compared to that of near IDTs, consistent with the numerical prediction. The results shown in Fig. 10(a) strongly indicate that our fabricated focusing IDTs are functioning as expected.

Figure 10(b) compares the transmission (S_{21}) of the PnC waveguide and the reference PnC structure using focusing IDTs [Figs. 6(a) and 6(b), respectively]. It is evident from Fig. 10(b) that the PnC structure considerably suppresses the acoustic-signal transmission at frequencies corresponding to its PnBG, where the waveguide structure shows a strong waveguiding effect (i.e., transmission) at frequencies corresponding to its excited guided mode.

To understand the effect of the polarization on the frequency response of the PnC waveguide, Fig. 11 shows the polarization and in-plane (anti)symmetry of the modes [5] supported by the fabricated waveguide, and it compares the frequency of these modes to the frequency response of the waveguide (WG) transmission normalized to that of the reference PnC structure. As expected, the high-transmission frequency range of the PnC waveguide corresponds to the single-mode frequency range of its AS mode that has in-plane symmetry (see the region identified by the dashed lines in Fig. 11). The measured maximum transmission at 1055 MHz is within 2% of the target wavgeuide mode (1067 MHz; see Fig. 5) obtained from numerical calculations. There are other in-plane symmetric modes with S polarization that can also contribute to the transmission response of the waveguide. However, we do not expect the

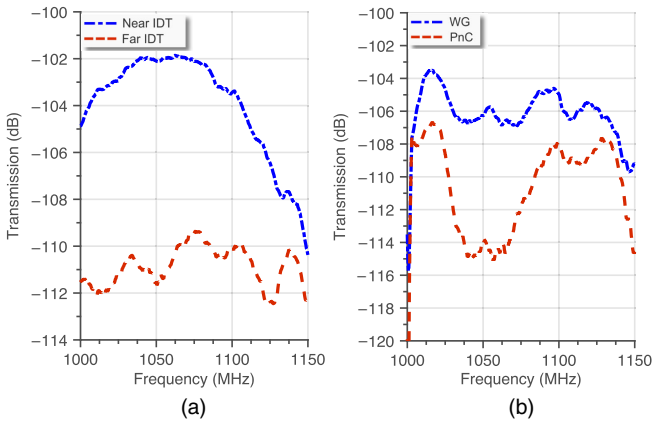

FIG. 10. Measured transmission (S_{21} parameter) of (a) the near and far focusing IDTs, whose designs are shown in Figs. 6(c) and 6(d), respectively, and (b) the far IDTs with the PnC waveguide and the PnC in between [Figs. 6(a) and 6(b), respectively].

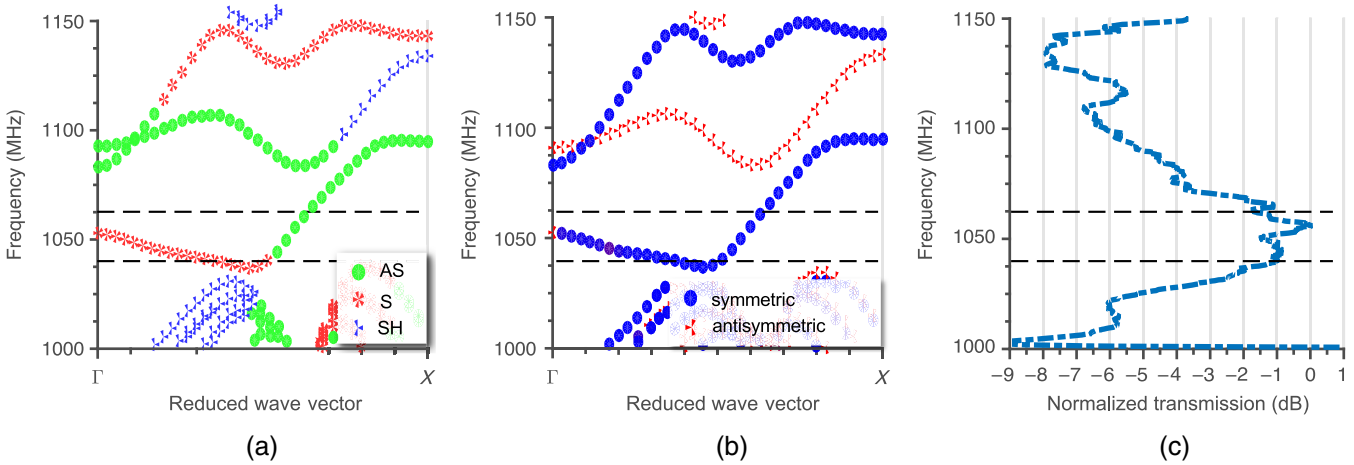

FIG. 11. Comparison of the dispersion diagram of (a) the types of the PnC waveguide modes [i.e., antisymmetric Lamb (AS), symmetric Lamb (S), and shear-horizontal (SH) waves] and (b) their symmetry or antisymmetry with respect to the in-plane perpendicular axis (z-axis in Fig. 5). (c) The measured normalized transmission of the fabricated waveguide in Fig. 9(a). The high-transmission window (i.e., 1040–1060 MHz) corresponds to the AS symmetric mode indicated by the horizontal dotted lines.

SH modes or the in-plane antisymmetric modes to have any effect on the waveguide transmission performance, as they are not excited by the focusing IDTs in Fig. 6.

VI. CONCLUSION

In this paper, we demonstrate a systematic approach for the design and the numerical analysis of PnC waveguides. A triangular-lattice PnC—composed of Ni pillars on a three-layer membrane of AlN, Mo, and Si—that supports a PnBG around 1100 MHz is designed to provide a platform for the design of a GHz PnC waveguide. Based on this design approach, we develop and optimize a PnC waveguide structure that supports a single guided mode around 1050 MHz. The optimization process includes careful selection of the geometrical dimensions of the PnC structure, as well as the frequency of operation that could easily be excited by the piezoelectric property of AlN. For the purpose of experimental demonstration of the waveguiding effect, we design and analyze an alternative type of focusing IDTs to facilitate the coupling of the elastic energy to the waveguide, and vice versa. Our experimental results corroborate our theoretical understanding of the physics of waveguiding and demonstrate the feasibility of waveguiding of elastic energy at GHz frequencies, a result that is in good agreement with our FEM simulations.

The practical requirement for low-loss PnCs, waveguides, and resonators demands a deeper physical understanding of and modeling techniques for loss mechanisms such as viscoelastic damping, thermoelastic loss, electronic processes affecting the material loss (especially in semiconductors), fabrication-imperfection-induced loss, and friction modeling for the contact surfaces between different layers of the device [28–32]. To have a robust signal-processing platform based on PnCs, all of these mechanisms should be understood to effectively model the micron- and submicron-scale structures to form more complex low-loss frequency-selective building blocks.

ACKNOWLEDGMENTS

This material is based upon work supported by the National Science Foundation under Grants No. ECCS-0901800 and No. ECCS-1310340. This work was performed in part at the Georgia Tech Institute for Electronics and Nanotechnology, a member of the National Nanotechnology Coordinated Infrastructure, which is supported by the National Science Foundation under Grant No. ECCS-1542174.

[1] T. T. Wu, Z. G. Huang, T. C. Tsai, and T. C. Wu, Evidence of complete band gap and resonances in a plate with periodic stubbed surface, Appl. Phys. Lett. **93**, 111902 (2008).

[2] Y. Pennec, B. Djafari Rouhani, H. Larabi, A. Akjouj, J. N. Gillet, J. O. Vasseur, and G. Thabet, Phonon transport and waveguiding in a phononic crystal made up of cylindrical dots on a thin homogeneous plate, Phys. Rev. B **80**, 144302 (2009).

[3] Mourad Oudich, Yong Li, Badreddine M. Assouar, and Zhilin Hou, A sonic band gap based on the locally resonant phononic plates with stubs, New J. Phys. **12**, 083049 (2010).

[4] Reza Pourabolghasem, Abdelkrim Khelif, Saeed Mohammadi, Ali Asghar Eftekhar, and Ali Adibi, Physics of band-gap formation and its evolution in the pillar-based phononic crystal structures, J. Appl. Phys. **116**, 013514 (2014).

[5] Reza Pourabolghasem, Saeed Mohammadi, Ali A. Eftekhar, Abdelkrim Khelif, and Ali Adibi, Experimental evidence of high-frequency complete elastic bandgap in pillar-based phononic slabs, Appl. Phys. Lett. **105**, 231908 (2014).

[6] Saeed Mohammadi, Ali A. Eftekhar, Reza Pourabolghasem, and Ali Adibi, Simultaneous high-Q confinement and selective direct piezoelectric excitation of flexural and extensional lateral vibrations in a silicon phononic crystal slab resonator, Sens. Actuators A **167**, 524 (2011).
[7] Saeed Mohammadi and Ali Adibi, Waveguide-based phononic crystal micro/nanomechanical high-Q resonators, J. Microelectromech. Syst. **21**, 379 (2012).
[8] Saeed Mohammadi and Ali Adibi, On chip complex signal processing devices using coupled phononic crystal slab resonators and waveguides, AIP Adv. **1**, 041903 (2011).
[9] Saeed Mohammadi, Ali Asghar Eftekhar, William D. Hunt, and Ali Adibi, High-Q micromechanical resonators in a two-dimensional phononic crystal slab, Appl. Phys. Lett. **94**, 051906 (2009).
[10] Razi Dehghannasiri, Reza Pourabolghasem, Ali Asghar Eftekhar, and Ali Adibi, Integrated phononic crystal resonators based on adiabatically-terminated phononic crystal waveguides, AIP Adv. **6**, 121603 (2016).
[11] Toyokatsu Miyashita and Chiryu Inoue, Numerical investigations of transmission and waveguide properties of sonic crystals by finite-difference time-domain method, Jpn. J. Appl. Phys. **40**, 3488 (2001).
[12] Jia-Hong Sun and Tsung-Tsong Wu, Propagation of acoustic waves in phononic-crystal plates and waveguides using a finite-difference time-domain method, Phys. Rev. B **76**, 104304 (2007).
[13] Paolo Celli and Stefano Gonella, Manipulating waves with Lego® bricks: A versatile experimental platform for metamaterial architectures, Appl. Phys. Lett. **107**, 081901 (2015).
[14] Mahmoud Addouche, Mohammed A. Al-Lethawe, Aliyasin Elayouch, and Abdelkrim Khelif, Subwavelength waveguiding of surface phonons in pillars-based phononic crystal, AIP Adv. **4**, 124303 (2014).
[15] Jia-Hong Sun and Tsung-Tsong Wu, Analyses of mode coupling in joined parallel phononic crystal waveguides, Phys. Rev. B **71**, 174303 (2005).
[16] Abdelkrim Khelif, Saeed Mohammadi, Ali Asghar Eftekhar, Ali Adibi, and Boujamaa Aoubiza, Acoustic confinement and waveguiding with a line-defect structure in phononic crystal slabs, J. Appl. Phys. **108**, 084515 (2010).
[17] Sz-Chin Steven Lin, Bernhard R. Tittmann, Jia-Hong Sun, Tsung-Tsong Wu, and Tony Jun Huang, Acoustic beamwidth compressor using gradient-index phononic crystals, J. Phys. D **42**, 185502 (2009).
[18] Sz-Chin Steven Lin, Tony Jun Huang, Jia-Hong Sun, and Tsung-Tsong Wu, Gradient-index phononic crystals, Phys. Rev. B **79**, 094302 (2009).
[19] Tsung-Tsong Wu, Yan-Ting Chen, Jia-Hong Sun, Sz-Chin Steven Lin, and Tony Jun Huang, Focusing of the lowest antisymmetric Lamb wave in a gradient-index phononic crystal plate, Appl. Phys. Lett. **98**, 171911 (2011).
[20] Tsung-Tsong Wu, He-Tai Tang, Yung-Yu Chen, and Pei-Ling Liu, Analysis and design of focused interdigital transducers, IEEE Trans. Ultrason. Ferroelectr. Freq. Control **52**, 1384 (2005).
[21] Vincent Laude, Davy Gérard, Naima Khelfaoui, Carlos F. Jerez-Hanckes, Sarah Benchabane, and Abdelkrim Khelif, Subwavelength focusing of surface acoustic waves generated by an annular interdigital transducer, Appl. Phys. Lett. **92**, 094104 (2008).
[22] Subramanian K. R. S. Sankaranarayanan and Venkat R. Bhethanabotla, Design of efficient focused surface acoustic wave devices for potential microfluidic applications, J. Appl. Phys. **103**, 064518 (2008).
[23] Zhaohong Wang, Tiantong Tang, Shi Chen, and Bing Chen, Field analysis and calculation of interdigital transducers with arbitrary finger shapes, J. Phys. D **39**, 4902 (2006).
[24] Bertram Alexander Auld, *Acoustic Fields and Waves in Solids*, 2nd ed., Vol. 1 (Wiley, New York, 1989).
[25] J. V. Sánchez-Pérez, D. Caballero, R. Martinez-Sala, C. Rubio, J. Sánchez-Dehesa, F. Meseguer, J. Llinares, and F. Gálvez, Sound Attenuation by a Two-Dimensional Array of Rigid Cylinders, Phys. Rev. Lett. **80**, 5325 (1998).
[26] F. L. Hsiao, A. Khelif, H. Moubchir, A. Choujaa, C. C. Chen, and V. Laude, Complete band gaps and deaf bands of triangular and honeycomb water-steel phononic crystals, J. Appl. Phys. **101**, 044903 (2007).
[27] Tzung-Chen Wu, Tsung-Tsong Wu, and Jin-Chen Hsu, Waveguiding and frequency selection of Lamb waves in a plate with a periodic stubbed surface, Phys. Rev. B **79**, 104306 (2009).
[28] A. Caron and W. Arnold, Observation of local internal friction and plasticity onset in nanocrystalline nickel by atomic force acoustic microscopy, Acta Mater. **57**, 4353 (2009).
[29] C. K. Jones and J. A. Rayne, Ultrasonic attenuation in tungsten and molybdenum up to 1 Gc/s, Phys. Lett. **13**, 282 (1964).
[30] Ze'ev Lindenfeld and Ron Lifshitz, Damping of mechanical vibrations by free electrons in metallic nanoresonators, Phys. Rev. B **87**, 085448 (2013).
[31] William Duffy, Jr., Acoustic quality factor of molybdenum and tungsten at low temperatures, J. Appl. Phys. **72**, 5628 (1992).
[32] Emmanuel P. Papadakis, Ultrasonic attenuation caused by scattering in polycrystalline media, Physical acoustics: principles and methods **4**, 269 (2012).